

Improved modeling of the solid-to-plasma transition of polystyrene ablator for laser direct-drive inertial confinement fusion hydrocodes

A. Pineau ^{1,*}, B. Chimier ¹, S. X. Hu ², and G. Duchateau ^{1,3,†}

¹*Université de Bordeaux-CNRS-CEA, Centre Lasers Intenses et Applications, UMR 5107, 351 Cours de la Libération, 33405 Talence Cedex, France*

²*Laboratory for Laser Energetics, University of Rochester, 250 East River Road, Rochester, New York 14623, USA*

³*CEA CESTA, 15 Avenue des Sablières, CS60001, 33116 Le Barp Cedex, France*



(Received 15 April 2021; accepted 25 June 2021; published 16 July 2021)

The target performance of laser direct-drive inertial confinement fusion (ICF) can be limited by the development of hydrodynamic instabilities resulting from the nonhomogeneous laser absorption at the target surface, i.e., the laser imprint on the ablator. To understand and describe the formation of these instabilities, the early ablator evolution during the laser irradiation should be considered. In this work, an improved modeling of the solid-to-plasma transition of a polystyrene ablator for laser direct-drive ICF is proposed. This model is devoted to be implemented in hydrocodes dedicated to ICF which generally assume an initial plasma state. The present approach consists of the two-temperature model coupled to the electron, ion and neutral dynamics including the chemical fragmentation of polystyrene. The solid-to-plasma transition is shown to significantly influence the temporal evolution of both free electron density and temperatures, which can lead to different shock formation and propagation compared with an initial plasma state. The influence of the solid-to-plasma transition on the shock dynamics is evidenced by considering the scaling law of the pressure with respect to the laser intensity. The ablator transition is shown to modify the scaling law exponent compared with an initial plasma state.

DOI: [10.1103/PhysRevE.104.015210](https://doi.org/10.1103/PhysRevE.104.015210)

I. INTRODUCTION

Laser direct-drive inertial confinement fusion consists in focusing high-energetic lasers onto a target to compress it and create nuclear fusion reactions [1–4]. Typical targets are usually made of a cryogenic deuterium-tritium (DT) shell filled with a gaseous DT mixture. The cryogenic DT shell is covered with a plastic layer, namely the ablator, which is often polystyrene [5]. By absorbing the laser energy, the ablator initially in a solid state is converted into a plasma and expands leading to the compression of the target through the so-called rocket effect. Intensity modulations coming from laser speckles or beam-to-beam interactions can lead to a nonhomogeneous laser absorption and density modulations at the target surface, which can be seeds of Rayleigh-Taylor and Richtmyer-Meshkov instabilities, i.e., the laser-imprinting process [6]. The latter reduces drastically ICF target performances [7–9]. To understand and control the formation of such instabilities, the ablator evolution during the laser irradiation should be taken into account, especially the solid-to-plasma transition.

The solid-to-plasma transition is generally neglected in ICF hydrocodes by assuming a negligible transition time compared with the total laser pulse duration. Simulations start with an ablator in the plasma state with an electron density higher than the critical density of the corresponding laser. However,

a recent study has shown that the timescale of this transition is of the order of 100 ps for a conventional laser pulse irradiation used in ICF [5], i.e., of the order of magnitude of the picket duration [10]. Moreover, the influence of the solid-to-plasma transition on the hydrodynamic processes, resulting from the laser absorption, has been highlighted by measuring the laser induced shock velocities in polystyrene [11]. Significant differences have been observed between experimental results and hydrodynamic simulations where the solid-to-plasma transition is not considered. Indeed, in the plasma state, the relative variations of the pressure scales linearly with the laser intensity following a linear absorption process, whereas a nonlinear behavior has been shown to be necessary to account for experimental observations [11]. This nonlinear behavior has been attributed to the primary step of plasma formation through two-photon absorption of polystyrene.

A first microscopic modeling of the solid-to-plasma transition has been proposed for a polystyrene ablator [5]. The ablator heating eventually leading to phase transition and plasma formation is evaluated owing to a two-temperature model describing the coupled evolution of both electron and lattice temperatures, and including the free electron density evolution induced by the laser irradiation. The free electron density is estimated by describing processes of photoionization, electron impact ionization, and electron recombination. Although this first microscopic modeling laid the foundations of the description of the solid-to-plasma transition, it must be improved for its introduction in a hydrocode due to several reasons. (i) The densities of carbon and hydrogen ions are not predicted whereas they are required to describe properly

*adrien.pineau@u-bordeaux.fr

†guillaume.duchateau@cea.fr

the plasma formation. The chemical fragmentation of initial solid polystyrene leading to atomic species has thus to be described (ii) The description of electron collisions is rather crude despite it provides correct orders of magnitude. To predict accurate electron and lattice heating (leading to phase transitions), a more accurate description of collisional processes is required. (iii) In the perspective of a model properly describing the material decomposition into a plasma where various transient chemical species are involved (electrons, polymer, molecules, atoms), adapted equations of state (EOS) have to be implemented.

The first goal of the present work is to introduce an improved microscopic modeling of the solid-to-plasma transition where the above-mentioned three assumptions of the first modeling attempt are fixed. The chemical fragmentation and improved collision frequencies are introduced following developments proposed in Ref. [12]. Both the energy transfer and the laser-induced electron dynamics, including photoionization, electron impact ionization, and electron recombination, are adapted to the state of matter. These theoretical developments are presented in Sec. II. Section III presents numerical simulations performed by using laser intensity profiles pertaining to ICF conditions. The solid-to-plasma transition is investigated where in particular the evolution of the chemical composition of the ablator is highlighted. Comparisons with typical initial conditions of ICF hydrocodes are also performed. The second goal of the present work is to address the evolution of the pressure as a function of the laser intensity following observations in Ref. [11]. A nonlinear behavior is evidenced in Sec. V confirming the role of the solid-to-plasma transition on the subsequent plasma hydrodynamics. Finally, conclusions and outlooks are drawn in Sec. VI. Owing to the fact it includes all main physical processes driving the solid-to-plasma transition, and provides densities and temperatures of formed plasma, the present model is devoted to be introduced in current hydrocode to improve their accuracy and correctly describe the onset of hydrodynamics which is expected to influence the subsequent implosion of ICF targets.

II. MODELING OF THE SOLID-TO-PLASMA TRANSITION

The phenomenology of the laser induced phase transition of a polystyrene ablator, i.e., chemical fragmentation, and its laser interaction are first summarized following a previous work [12] to introduce the forthcoming theoretical developments. Let define T_{il} the temperature of the so called ion-lattice system [5] which includes various chemical species as polymer, molecules, or atoms with different ionization degree [12]. If $T_{il} < 58$ meV, then the ablator is constituted of solid polystyrene which is a polymer. In that case, there is a band structure constraining the electron dynamics, and the electrons undergo collisions with phonons. If $T_{il} > 58$ meV, then the ablator consists of several species, namely styrene, benzene, acetylene molecules, or carbon and hydrogen atoms, with various ionization degrees, depending on temperatures. In that case, the electron dynamics consists of successive ionizations of these molecules and atoms. Within this phase, electrons undergo collisions with ions and neutral species. As

a final product of the laser induced and thermal molecule dissociations, the ablator consists of a mixture of ionized carbon and hydrogen atomic species (i.e., at the end of the solid-to-plasma transition). Such a scenario for the chemical fragmentation of polystyrene implies that laser induced electron dynamics, electron collision frequencies, and energy transfer between various species populations, have to be adapted to a given chemical composition which depends on ion-lattice temperature.

For typical laser pickets used in ICF experiments, i.e., Gaussian profile with a maximum laser intensity about 10^{14} W.cm⁻² and a duration of 100 ps, the solid-to-plasma takes place over a timescale of about 100 ps [5] which is smaller than the hydrodynamic timescale. Hydrodynamic processes can thus be neglected *a priori* (based on the forthcoming results, an estimation of the hydrodynamic expansion will confirm this assumption *a posteriori*). In addition, thermal diffusion is also neglected. The smallest spatial scale where absorption is not uniform corresponds to the intensity profile of one laser speckle which characteristic size is of the order of 1 μ m. Due to the variations of absorption and energy deposition on this spatial scale, the resulting temperature gradient may lead to thermal diffusion in general. By using the expression of thermal conductivity provided in Ref. [12], calculations show that the characteristic diffusion time becomes short enough (~ 1 ps) to induce heat diffusion only when the solid-to-plasma transition is finished, i.e., when a fully plasma state is formed. Heat diffusion thus can be neglected during the solid-to-plasma transition.

The ablator is a system out of equilibrium (temperatures of electrons and ion-lattice are different in general) during the solid-to-plasma transition since electrons are first excited by the laser, and the ion-lattice system is then heated subsequently through electron collisions which transfer their energy. The evolution of the electron and ion-lattice temperatures (T_e and T_{il} , respectively) is modeled with the two-temperature model, which reads

$$C_e \frac{\partial T_e}{\partial t} = -\tilde{\mu}_e \frac{\partial n_e}{\partial t} - \left(\frac{\partial U_e}{\partial t} \right)_{\text{collisions}} + \left(\frac{\partial U_e}{\partial t} \right)_{\text{laser}}, \quad (1)$$

$$C_{il} \frac{\partial T_{il}}{\partial t} = - \sum_s \tilde{\mu}_s \frac{\partial n_s}{\partial t} + \left(\frac{\partial U_e}{\partial t} \right)_{\text{collisions}}, \quad (2)$$

where ions and neutral species are assumed to have the same temperature. C_e and C_{il} correspond to the electron and ion-lattice heat capacities, respectively. The first term in the right hand side of both equations correspond to the variation of energy due to the evolution of the number of particules ($\tilde{\mu}_e$ and $\tilde{\mu}_s$ are effective chemical potentials and the sum is over the different chemical species constituting the ion-lattice system; see Appendix A). The second terms account for the energy transfer from the electrons to the ion-lattice system due to electron collisions. The last term in Eq. (1) corresponds to the laser heating. Except C_e and $(\partial_t U_e)_{\text{laser}}$ which exhibit generic expression, all the quantities appearing in Eqs. (1) and (2) depend on the chemical composition of the ablator and have to be defined according to the ion-lattice temperature.

A. Laser heating

The laser energy absorbed by electrons $(\partial_t U_e)_{\text{laser}}$ is given by the Drude model [5]:

$$\left(\frac{\partial U_e}{\partial t}\right)_{\text{laser}} = \frac{e^2 n_e v_c}{m_e (\omega_L^2 + v_c^2)} E_L^2, \quad (3)$$

where ω_L and E_L are the laser frequency and laser electric field, respectively. The electron collision frequency v_c is given by a model dedicated to the solid-to-plasma transition of the polystyrene ablator [12]. If the lattice-ion temperature is smaller than 58 meV, then v_c is evaluated from collisions between electrons and both acoustic and optical phonons of solid polystyrene. This collision frequency is evaluated with the Fermi golden rule. If the lattice-ion temperature is higher than 58 meV, then electron-ion collisions take place, which are described by the Lee & More model [13] using the average collision time. A Coulomb logarithm different from the Lee & More model is used [14] since collisions may take place in a strongly coupled regime for electron temperatures of a few eV. We have checked by evaluating the electron and ion coupling parameter that such an estimation for the Coulomb logarithm is suitable for the solid-to-plasma transition. Electron-neutral collisions are described by using classical cross sections.

B. Equations of state

The electron heat capacity C_e and the effective chemical potential $\tilde{\mu}_e$ are evaluated for both $T_{il} < 58$ meV and $T_{il} > 58$ meV from the general free electron gas equation of state which includes both degenerated limit and ideal gas behavior for temperatures larger than the Fermi temperature (see Appendix B). The ion-lattice heat capacity C_{il} and the ion-lattice effective chemical potential $\tilde{\mu}_s$ depend on the considered species and thus depend on the ion-lattice temperature.

For $T_{il} < 58$ meV, C_{il} is the heat capacity of solid polystyrene. In that case, $C_{il} = C_m \rho / M$ with $M = 104$ g.mol⁻¹ and $\rho = 1.1$ g.cm⁻³ the styrene molecular mass and polystyrene density, respectively. The molar heat capacity C_m of polystyrene, which depends on the lattice temperature, is given by a fit of experimental data [15]. $\tilde{\mu}_s$ is associated to the variation of the polystyrene energy due to the variation of the phonon density. Because the internal energy of polystyrene does not depend on the phonon density [16], it comes directly $\tilde{\mu}_s = 0$.

For $T_{il} > 58$ meV, C_{il} corresponds to the heat capacity of both ions and neutrals (molecular and atomic species). Because a same temperature is assumed, $C_{il} = C_i + C_n$ with C_i and C_n the heat capacity of ions and neutrals, respectively. C_i is deduced from the Cowan model [17] which is a standard equation of state used in ICF. For neutrals, an ideal gas is assumed, i.e., $C_n = 3k_B n_n / 2$ with n_n the total density of neutrals.

The effective chemical potential of ions and neutrals, $\tilde{\mu}_s$, is given from the same EOS as the one used for the heat capacities, see Appendix A.

Note that relatively simple EOS are used in this model, in particular for neutrals. Forthcoming results of Sec. III shows that neutrals exist only during a short period of time. Thus, a more suitable EOS for neutrals is not expected to change the results and conclusions of this work. For electrons and

ions, the thermal energy was compared to the Fermi energy and the interaction potential. It turned out that screening and quantum effects can be neglected during the solid-to-plasma transition. In addition, the presently used EOS have been compared (results not shown) with *ab initio* calculations [18] providing the evolution of the pressure with respect to the temperature at equilibrium ($T_e = T_i$). A good agreement is obtained, definitively confirming the EOS used in this model is suitable for the description of the solid-to-plasma transition.

C. Electron dynamics

Photoionization, electron impact ionization, and electron recombination are general processes taking place for all matter composition: polymer, molecules, or atoms. However the formalism used to describe these processes depends on the transient chemical composition, i.e., on the ion-lattice temperature T_{il} . When the ablator species are molecules and atoms ionized or not, the dissociation of molecules has further to be considered.

1. Conditions where $T_{il} < 58$ meV

The ablator is solid polystyrene which is a polymer, i.e., a dielectric material. The band structure consists of two bands, the valence band (VB) and the conduction band (CB), separated by a bandgap of 4.05 eV [19]. Before any interaction, most of the electrons are in the VB while a small number is in the CB. Because a polystyrene target with a temperature different from zero is considered, the CB is initially populated with an electron density of the order of 10^{10} cm⁻³ [20]. Due to photoionization, electrons in the VB are promoted into the CB. Promoted electrons in the CB may reach higher energy levels by successive one-photon absorption. When the energy level becomes higher than the bandgap energy, those electrons may collide valence electrons resulting in two electrons in the bottom of the CB. The latter process is the so called electron impact ionization in dielectric materials [21]. In solid polystyrene, three levels of the CB have thus to be considered [5]. Accounting for these two ionization processes and electron recombination, the laser-induced electron dynamics can be described as follows [5]:

$$\frac{\partial n_0}{\partial t} = \alpha W_{PI} + 2\alpha v_{II} n_2 - W_1 n_0 - v_r (n_0 - n_{cb0}), \quad (4)$$

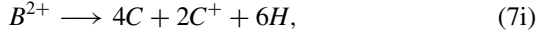
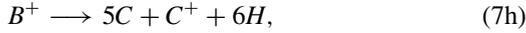
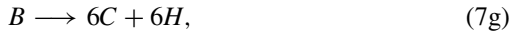
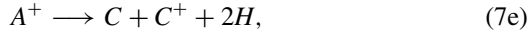
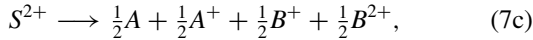
$$\frac{\partial n_1}{\partial t} = W_1 n_0 - W_1 n_1 - v_r n_1, \quad (5)$$

$$\frac{\partial n_2}{\partial t} = W_1 n_1 - \alpha v_{II} n_2 - v_r n_2, \quad (6)$$

where n_0 , n_1 , and n_2 correspond to the electron densities in the three levels considered in the CB and n_{cb0} the initial electron density of the CB. $v_{II} = 10^{14}$ s⁻¹ and $v_r = 10^{12}$ s⁻¹ correspond to the electron impact ionization and recombination frequencies, respectively. The photoionization rate W_{PI} is evaluated with the Keldysh theory accounting for both tunnel ionization and multiphoton absorption [22]. The one-photon absorption rate is set to $W_1 = 10^{-7} E_L^2$, in units of s⁻¹, where E_L is the laser electric field [5]. Finally, $\alpha = 1 - (n_0 + n_1 + n_2) / n_{vb0}$, with n_{vb0} the initial electron density in the VB, accounts for the depletion of the VB.

2. Conditions where $T_{il} > 58$ meV

For this range of temperatures, the electron dynamics corresponds to the successive ionizations and dissociations of the molecular and atomic species. Within the ICF framework, the chemical species involved in the chemical fragmentation of the ablator are styrene, benzene, acetylene, carbon, and hydrogen [12]. Both neutral and ionized forms have to be considered for each species to model the plasma formation. The following mixture is thus considered: $S, S^+, S^{2+}, A, A^+, A^{2+}, B, B^+, B^{2+}, H, H^+, C, C^+, C^{2+}, C^{3+}, C^{4+}, C^{5+}, C^{6+}$, where S, A, B, H , and C correspond to styrene, acetylene, benzene, hydrogen, and carbon, respectively. The density evolution of those species is related to the electron dynamics including photoionization, electron impact ionization, and electron recombination. Dissociations of styrene, benzene and acetylene molecules must also be described to model the chemical fragmentation of the ablator. The most relevant dissociations reactions are [12]



which take place when the ion-lattice temperature is about several eV. The dynamics of each population is described as follows:

$$\frac{\partial n_{X^j}}{\partial t} = \sum_s Q_{D,s} + Q_{\text{IR}}(X^{j-1} \leftrightarrow X^j) - Q_{\text{IR}}(X^j \leftrightarrow X^{j+1}), \quad (8)$$

with $X \in \{S, A, B, H, C\}$ denoting the chemical species and $j \geq 0$ the ionization state. The first term corresponds to the dissociation rate where the sum is over all the reactions driving the evolution of the population X . For example, in the case of B^+ , three dissociations rates have to be considered accounting for the reactions (7b), (7c), and (7h). The dissociation rate reads

$$Q_D = \beta n_D k_{\text{arr}} \exp\left(-\frac{E_a}{k_B T_{il}}\right), \quad (9)$$

with β the algebraic stoichiometric coefficient (negative for reactants, positive for products), n_D the density of the molecule that dissociates, k_{arr} the Arrhenius law prefactor, and E_a the activation energy. We set $k_{\text{arr}} = 10^{13} \text{ s}^{-1}$ corresponding to the characteristic time of dissociation of a molecule [23]. For the reactions given by Eqs. (7a)–(7c), one has $E_a = 2.4$ eV and for the reactions given by Eqs. (7d)–(7i), $E_a = 6$ eV [12]. The second and third term in Eq. (8) correspond to the transitions between the $j - 1$ th and j th ionization state, and the j th and the $j + 1$ th ionization state, respectively. It is assumed

that these transitions can be due to photoionization (PI), electron impact ionization (EII), and electron recombination (ER) leading to

$$\begin{aligned} Q_{\text{IR}}(X^{j-1} \leftrightarrow X^j) &= W_{\text{PI}}(X^{j-1} \rightarrow X^j)n_{X^{j-1}} + W_{\text{EII}}(X^{j-1} \\ &\rightarrow X^j)n_{X^{j-1}} - W_{\text{ER}}(X^j \rightarrow X^{j-1})n_{X^j}. \end{aligned} \quad (10)$$

Photoionization of carbon and hydrogen atomic species is described within the Keldysh formalism for atoms [22]. To get a tractable model, this Keldysh expression derived for atoms is also used to calculate the photoionization rate of styrene, benzene and acetylene, assuming the ionization energy is the main parameter driving the electron dynamics. Electron impact ionization is described with the Gryziński's theory [24] as a compromise between simplicity and accuracy. Concerning electron recombination, the approach of Zel'dovich [25] is adapted by substituting the Coulomb potential by the Debye-Hückel potential to account for screening effects which are significant at solid density:

$$W_{\text{ER}}(X^j \rightarrow X^{j-1}) = \pi^2 n_e^2 j^3 \sqrt{\frac{8k_B T_e}{\pi m_e}} \left[\lambda_D W\left(\frac{2e^2}{3\lambda_D k_B T_e}\right) \right]^5, \quad (11)$$

where $\lambda_D = \sqrt{k_B T_e / 4\pi n_e e^2}$ is the screening Debye length and W is the principal branch of the W -Lambert function.

The evaluation of the density of each population with Eq. (8) allows us to define the densities of electrons n_e , ions n_i , and neutrals n_n :

$$n_e = \sum_{X,j \geq 1} Z_j n_{X^j}; \quad n_i = \sum_{X,j \geq 1} n_{X^j}; \quad n_n = \sum_X n_X, \quad (12)$$

where Z_j is the charge of the ion n_{X^j} , and the total density is given by $n_T = n_i + n_n$.

D. Energy transfer

When $T_{il} < 58$ meV, the ablator is solid polystyrene and the energy transfer is mainly due to electron-phonon collisions. When $T_{il} > 58$ meV, the ablator is constituted of molecules and atoms. In that case the energy transfer is mainly supported by electron-ion collisions.

For $T_{il} < 58$ meV, as a first approximation, it is possible to assume that two optical phonons with energy $\hbar\omega_{LO,1} = 33$ meV and $\hbar\omega_{LO,2} = 88$ meV, and one acoustic phonon exist in polystyrene [12]. Thus, the energy transfer from electrons to phonons is given by

$$\left(\frac{\partial U_e}{\partial t}\right)_{\text{collisions}} = \left(\frac{\partial U_e}{\partial t}\right)_{\text{AC}} + \left(\frac{\partial U_e}{\partial t}\right)_{\text{LO,1}} + \left(\frac{\partial U_e}{\partial t}\right)_{\text{LO,2}}, \quad (13)$$

accounting for the different contributions of each phonon. The electron-acoustic phonon and electron-optical phonon energy

transfer are respectively defined by

$$\left(\frac{\partial U_e}{\partial t}\right)_{AC} = \nu_{et,ac} n_e k_B (T_e - T_{il}), \quad (14)$$

$$\left(\frac{\partial U_e}{\partial t}\right)_{LO} = \nu_{et,op} \hbar \omega_{LO} n_e [g(T_e) - g(T_{il})], \quad (15)$$

where $g(T) = [\exp(\hbar \omega_{LO}/k_B T) - 1]^{-1}$ corresponds to the Bose-Einstein distribution and $\nu_{et,ac}$ and $\nu_{et,op}$ are the energy transfer frequencies evaluated in Appendix C.

For $T_{il} > 58$ meV, the ablator is constituted of molecules and atoms. Because they are mostly ionized due to the laser, the energy transfer is mainly due to electron-ion interactions which is described by the energy transfer derived by Landau [26]:

$$\left(\frac{\partial U_e}{\partial t}\right)_{\text{collisions}} = \frac{4n_e n_i Z^2 e^4 \sqrt{2\pi m_e} \ln \Lambda}{m_{\text{eff}} (k_B T_e)^{3/2}} k_B (T_e - T_{il}), \quad (16)$$

where $m_{\text{eff}} = (\sum_{X,j} m_{Xj} n_{Xj}) / (\sum_j n_{Xj})$ is the effective mass of ions. It accounts for the variation of the mass of ions due to the dissociation of the molecular species. In Λ corresponds to the Coulomb logarithm for which an approximation valid for dense plasmas is used [14]. Note that the energy transfer between electrons and neutral species is neglected. This is supported by the fact that neutrals are only present during a short period of time as shown in Sec. III.

III. RESULTS ON THE DYNAMICS OF THE SOLID-TO-PLASMA TRANSITION

To perform numerical calculations with the model presented previously, a 351-nm laser is considered with a temporal Gaussian shape $I(t) = I_0 \exp(-4 \ln 2 (t - t_{\text{max}})^2 / \tau^2)$ where I_0 , t_{max} and τ are chosen such that they correspond to typical laser picket parameters used in ICF experiments [27]. This leads to $I_0 = 10^{14} \text{ W.cm}^{-2}$, $t_{\text{max}} = 200$ ps and $\tau = 100$ ps. The initial temperature for electrons and the ion-lattice system is set to 300 K. Simulations begin when the laser intensity is high enough to quickly produce an electron density in the CB of the order of the initial electron density (10^{10} cm^{-3}), i.e., when the laser beam modifies significantly the material. Calculations are stopped when the electron density remains constant, ensuring the solid-to-plasma transition is ended since no more electrons can be generated. It then turns out that simulations are performed between -75 ps and 100 ps. The laser is already intense enough for $t < 0$ ps to create a significant free electron density, and the electron density remains constant after $t > 100$ ps.

Figure 1 shows the temporal evolution of the electron density, electron and ion-lattice temperatures, and the electron collision frequency between -75 ps and 100 ps.

Regarding the electron density, a monotonic behavior is observed when $t < 50$ ps. The ablator is solid polystyrene, this variation of the electron density is driven by the photoionization process. The electron impact ionization has a weak influence because the laser is not intense enough to promote a high number of electrons to the third level and initialize the electron breakdown. For $t > 50$ ps, the ablator is constituted of molecules and atoms and the electron generation is driven by electron impact ionization. The ionization energies of the

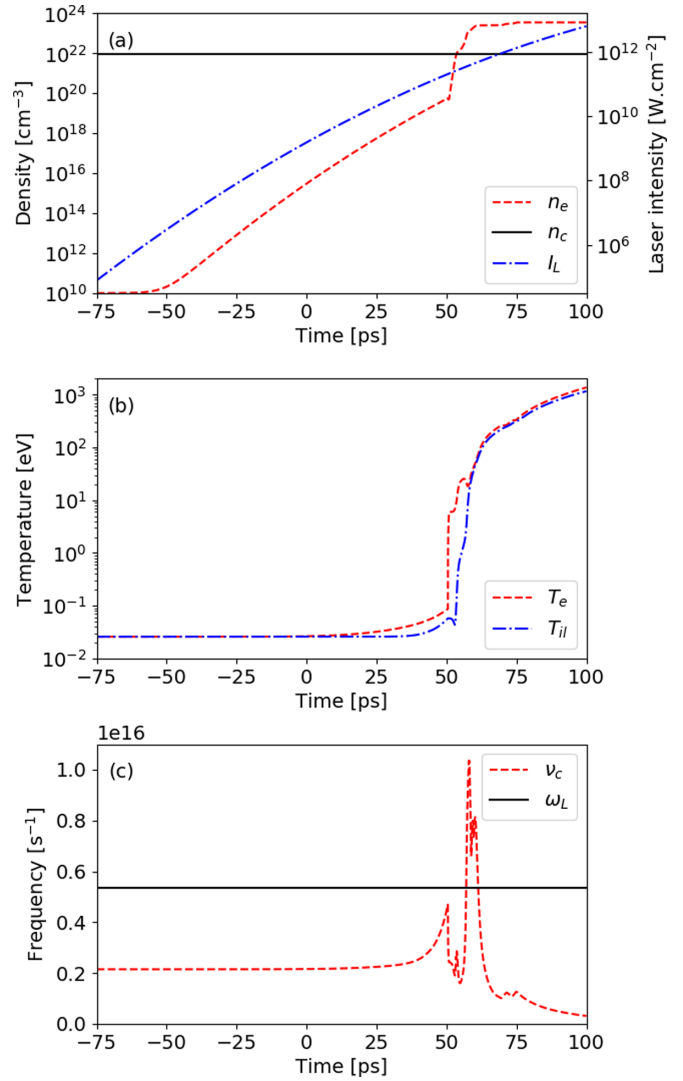


FIG. 1. Evolution of (a) the electron density n_e and the laser intensity I_L , (b) electron temperature T_e and ion-lattice temperature T_{il} , and (c) the electron collision frequency ν_c as a function of time. The critical density $n_c = m_e \omega_L^2 / 4\pi e^2$ and the laser frequency ω_L are given for purpose of comparison. A Gaussian profile is considered for the laser intensity with a maximum of $10^{14} \text{ W.cm}^{-2}$ reached at 200 ps and a duration of 100 ps.

species constituting the ablator are about 8 eV for the lowest one, simultaneous absorption of three photons is required to photoionize which makes this rate low. Since the electron temperature is higher than 10 eV for $t > 50$ ps, the impact ionization process becomes dominant. The first increase of the electron density going from $n_e \approx 6 \times 10^{19} \text{ cm}^{-3}$ to $n_e \approx 10^{22} \text{ cm}^{-3}$ corresponds to the ionization of styrene molecules since the ion-lattice system remains cold and only styrene molecules are present. The second increase where the electron density goes from $n_e \approx 10^{22} \text{ cm}^{-3}$ to $n_e \approx 2.5 \times 10^{23} \text{ cm}^{-3}$ correspond to the simultaneous ionizations of benzene, acetylene, hydrogen and carbon atomic species. The ion-lattice temperature increases from 0.1 to 10 eV and all the dissociation reactions given by Eqs. (7a)–(7i) take place. Finally, the last two increases of the electron density taking place between

70 and 75 ps are associated to the fifth and sixth ionization of atomic carbon. The ion-lattice temperature is about a few hundreds of eV and the ablator is mostly composed of hydrogen and carbon atomic species. When $n_e \approx 3.5 \times 10^{23} \text{ cm}^{-3}$, all the species are fully ionized, no more electrons can be generated and the electron density remains constant. Thus, the initial solid ablator has transformed into a fully ionized plasma, and the solid-to-plasma transition can be considered as finished. Note that as long as $t < 54$ ps, the electron density is smaller than the critical density. For these early times where the intensity is lower than a few $10^{11} \text{ W.cm}^{-2}$, the laser beam can propagate throughout the ablator and be absorbed in the fuel area [28]. This is the shined-through issue which may reduce the target efficiency [5,29].

Concerning the temperatures and the electron collision frequency, two behaviors associated to $t < 50$ ps and $t > 50$ ps can be noticed, as for the electron density evolution. For $t < 50$ ps, electrons remain relatively cold, the electron temperature does not exceed 0.1 eV. Although the electron collision is important, $\nu_c \approx 2 \times 10^{15} \text{ s}^{-1}$, leading to an efficient laser heating, the energy transfer from electrons to the lattice is also important and the whole laser energy acquired by the electrons is directly transferred to the lattice. This results in a slow increase of the electron temperature. However, even if the internal energy of the lattice increases due to the electron-phonon energy transfer, it does not lead to a significant heating of the lattice due to the large value of the polystyrene heat capacity.

For $t \approx 50$ ps, the electron temperature increases rapidly due to the drop of the energy transfer. At this moment where $T_{il} \approx 58 \text{ meV}$, the chemical constitution of the ablator changes going from solid polystyrene to styrene which is a molecular specie. The nature of the energy transfer is modified because collisions are no longer between electrons and phonons but between electrons and ions. This drop of the energy transfer leads to a heating of the ions much less efficient and the ion-lattice temperature decreases because, however, the internal energy of styrene is modified due to ionization. Note that a signature of the phase transition is the drop of the electron collision frequency at $t \approx 50$ ps.

For $t > 50$ ps, the electron temperature and the ion-lattice temperature increase due to the laser heating and electron-ion energy transfer, respectively. Regarding the behavior of the electron collision frequency, it first increases because the electron density increases due to ionization while the electron temperature remains relatively constant around 10 eV. Then, the electron collision frequency decreases because the electron density does not increase much going from $2.5 \times 10^{23} \text{ cm}^{-3}$ to $3.5 \times 10^{23} \text{ cm}^{-3}$ while the electron temperature increase significantly.

To have a closer look at the evolution of the chemical composition of the ablator in the plasma state, Fig 2 shows the temporal evolution of the density of styrene, acetylene, benzene molecules, and the density of hydrogen and carbon atomic species during the solid-to-plasma transition. They are shown between $t \approx 50$ ps (moment when polystyrene dissociates into styrene molecules) and $t \approx 60$ ps (densities of benzene and acetylene molecules are small enough so that only carbon and hydrogen atomic species remain). Such a temporal window ensures to capture the entire chemical fragmentation of the ablator.

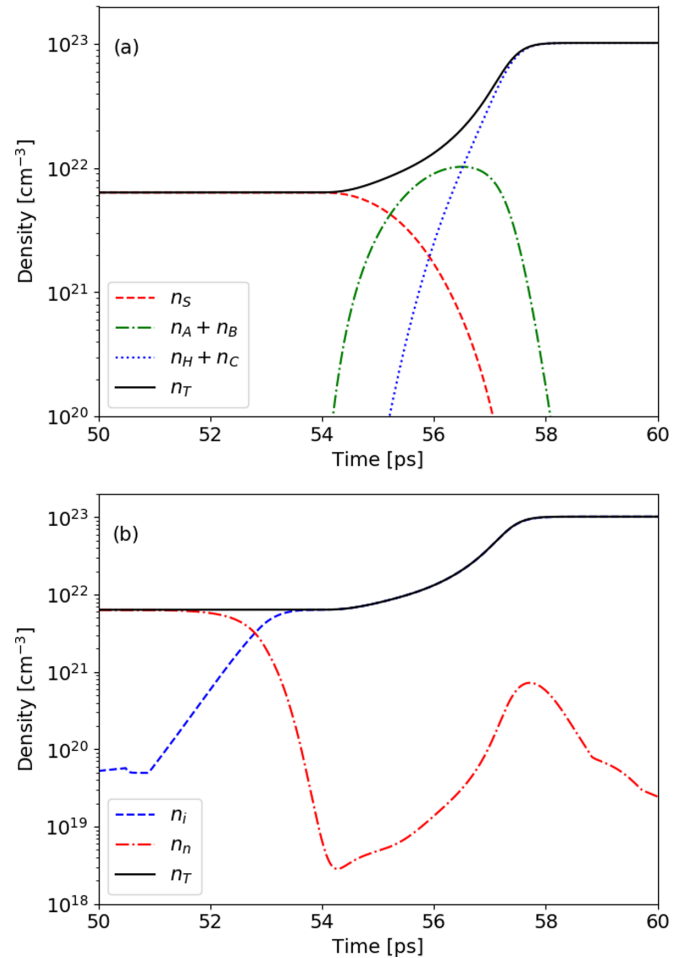


FIG. 2. (a) Temporal evolution of the density of styrene molecules n_S , acetylene molecules n_A , benzene molecules n_B , hydrogen atoms n_H , carbon atoms n_C , and the total density n_T . The evolution of n_A and n_B as well as n_H and n_C are plotted together because they appear and disappear for the same ion-lattice temperature (see Sec. II C 2). For each specie, the density corresponds to the density of neutrals plus the density of ions. (b) Temporal evolution of the total ion density n_i , total neutral density n_n and the total density $n_T = n_i + n_n$. As a reminder, the total ion and neutral densities n_i and n_n are defined by Eq. (12). The same laser intensity profile as the one used for Fig. 1 is considered.

Because the ion-lattice temperature increases during the solid-to-plasma transition, the ablator is successively constituted of polystyrene, styrene molecules, benzene, and acetylene molecules, and finally carbon and hydrogen atomic species. This chemical fragmentation can be observed with the increase of the total density on a timescale of ~ 10 ps which is not negligible compared with the whole solid-to-plasma transition timescale of ~ 100 ps [5]. Thus, the chemical fragmentation of the ablator cannot be neglected in the description of the solid-to-plasma transition. However, benzene and acetylene are only present during a few picoseconds. This is due to the fact that the ion-lattice temperature increases very quickly from 0.1 eV to several tens of eV. Thus, as a possible increase in computational efficiency for purposes of implementation in a hydrocode, it could be assumed that

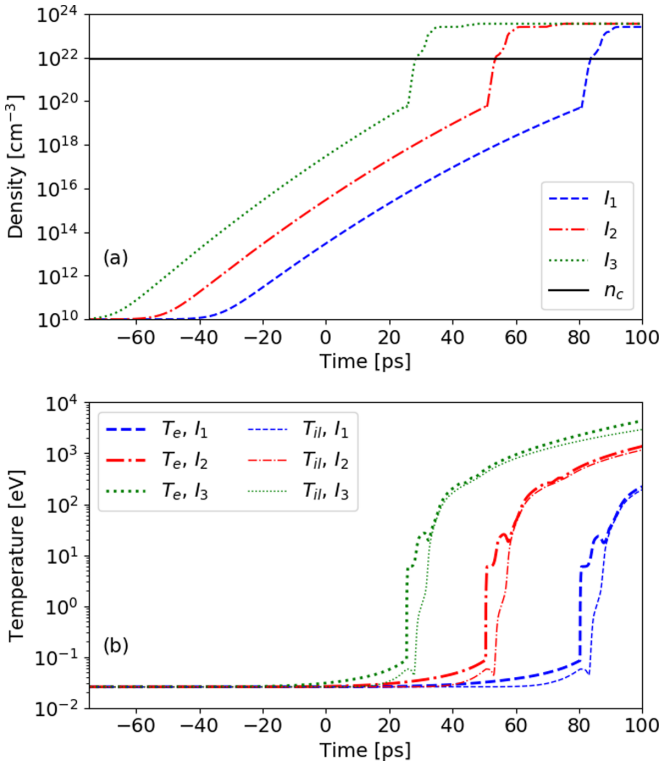


FIG. 3. (a) Evolution of the electron density as a function of time. (b) Evolution of the electron temperature T_e (thick lines) and the ion-lattice temperature T_{il} (thin lines) as a function of time. Simulations are performed with a Gaussian laser shape with a duration of 100 ps for the three following maximum laser intensities $I_1 = 10^{13} \text{ W.cm}^{-2}$, $I_2 = 10^{14} \text{ W.cm}^{-2}$, and $I_3 = 10^{15} \text{ W.cm}^{-2}$ reached at 200 ps. For the temperatures, solid and dashed lines corresponds to electron and ion-lattice temperatures respectively. The critical density n_c is shown for purpose of comparison.

styrene dissociates directly into carbon and hydrogen atomic species.

Regarding the temporal evolution of neutral and ionized species, neutrals exist only during a very short period of time compared to the solid-to-plasma transition timescale. Just after the polystyrene dissociation, the ablator is mainly composed of neutrals molecules. Because the electron temperature is small at this moment, there is no impact ionization. The latter process starts when electrons are hot enough, then neutral and ion densities decreases and increases, respectively. After a fast decrease between $t = 52$ ps and $t = 54$ ps because of the ionization of styrene molecules, the neutral density increases between $t = 54$ ps and $t = 58$ ps. This is due to the chemical fragmentation of the ablator which leads to the formation of new neutral species. Regarding chemical reactions given by Eqs. (7a)–(7i), it can be observed that neutral species are created during the dissociation of ions. Finally, the neutral density decreases again for $t > 58$ ps because the chemical fragmentation is ended. Neutrals species do no longer appear and already present neutrals disappear because they are ionized by electron impact. Even though neutrals are present during a short period of time, considering them enable not to have to use some tweaks to properly describe the solid state transition to a mixture of ionic species. This approach

TABLE I. Solid-to-plasma transition timescale as a function of the maximum laser intensity.

Maximum laser intensity [W.cm^{-2}]	10^{13}	10^{14}	10^{15}
Solid-to-plasma transition timescale [ps]	125	110	100

ensures the continuity of the quantities such as the electron collision frequency.

The solid-to-plasma transition timescale as predicted by this improved model is now addressed. Figure 3 shows the temporal evolution of the electron density and both electron and ion-lattice temperatures for three maximum laser intensities I_0 commonly used in ICF experiments [27]. The solid-to-plasma transition timescale is defined as the duration necessary to fulfill two criteria: $n_e \geq n_c$ and $T_{il} \geq 0.1$ eV. The second criterion ensures the periodicity of the lattice is broken (plasmas in general are disordered matter). Figure 3 shows that the temporal shape of n_e , T_e and T_{il} during the solid-to-plasma transition does not depend on the maximum laser intensity, it mainly consists of a temporal shift. However, the laser intensity has a slight influence on the solid-to-plasma transition timescale as summarized in Table I. More intense is the laser, more energy is absorbed by the ablator, and faster the plasma state is reached. The presently obtained timescale is consistent with previous estimations providing ~ 100 ps [5]. Indeed, the ablator remains a relatively long time in the solid state before undergoing any phase transition, the electron dynamics is mainly driven by photoionization of polystyrene. Thus, electron impact ionization taking place when the ablator is constituted of molecules and atomic species has only a weak influence on the solid-to-plasma transition timescale.

IV. COMPARISON TO THE INITIAL PLASMA CONDITIONS ASSUMED IN CURRENT HYDROCODES

The model introduced in this work is now compared with initial conditions corresponding to a fully ionized carbon-hydrogen plasma. These are standard initial conditions used in ICF hydrocodes where in particular the electron density is over critical. The present model is also compared with the one introduced by Duchateau *et al.* [5]. For the three models, the initial temperature of electrons and ions is 300 K and a Gaussian laser pulse with the same parameters as previously is used. Figure 4 provides the temporal evolution of the electron density, the electron temperature and the ion-lattice temperature as predicted by the three approaches.

Regarding the electron density, the model presented in this work and the one developed by Duchateau *et al.* give similar results as long as $t < 50$ ps, i.e., when solid polystyrene still stands, because the same description of the electron dynamics (photoionization with band structure) is used in both models. For $t > 50$ ps where chemical fragmentation takes place, the disagreement is due to the fact that Duchateau *et al.* still assume the same model for electron dynamics as previously whereas impact ionization of molecules and atoms becomes significant. Since the present improved model accounts for full ionization, the electron density of the initial plasma model ($\sim 3.5 \times 10^{23} \text{ cm}^{-3}$) is retrieved.

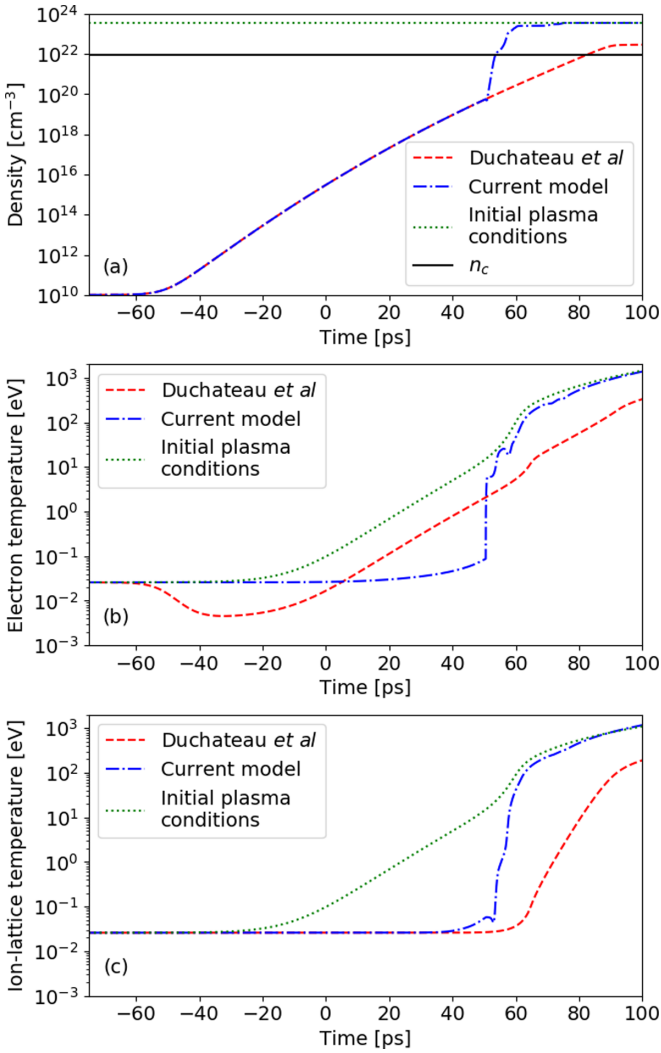


FIG. 4. Electron density (a), electron temperature (b), and ion-lattice temperature (c) during the solid-to-plasma transition evaluated for different models. The red curve corresponds to the model developed by Duchateau *et al.* [5]. The blue curve corresponds to the model presented in this work. The green curve corresponds to initial conditions that can be encountered in current hydrocodes, i.e., the ablator is assumed to be initially a fully ionized carbon-hydrogen plasma. The same laser intensity profile as the one used in Sec. III is considered.

Considering electron and ion-lattice temperatures at the end of the solid-to-plasma transition, similar results are obtained from our improved model and from the case where the ablator is assumed to be initially a fully ionized plasma. Because the laser absorption by the ablator leading to the electron generation and the chemical fragmentation of the ablator takes place for laser intensities much smaller than those associated to the heating of the electrons and the ion-lattice system when the ablator is totally ionized, the total laser energy absorbed by the ablator is about the same whether the solid-to-plasma transition is considered or not. However the initially fully ionized plasma leads to an ablator heated earlier since the electron density is much higher at the beginning of the interaction, which makes more efficient the laser heating of electrons and the electron-ion energy transfer. We thus expect that the ablator expansion takes place later when

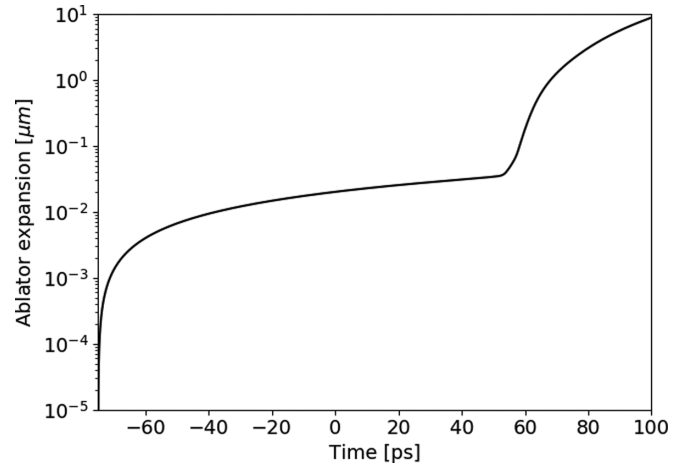


FIG. 5. Ablator expansion during the solid-to-plasma transition. The same laser intensity profile as the one used in Sec. III is considered.

the solid-to-plasma transition is considered. Compared with the first attempt of model of solid-to-plasma transition, the interest of the present model is clearly shown by the differences in electron and ion temperatures. This discrepancy is due to improved model of collision frequencies and chemical fragmentation affecting the electron dynamics.

Compared with an initial plasma state, previous results have shown that accounting for the solid-to-plasma transition is expected to modify electron density and transient temperatures which drive both the laser dynamics and shock wave formation. Such conclusions were drawn assuming no hydrodynamics. This assumption can now be evaluated *a posteriori* to confirm previous predictions. For this purpose, the ablator expansion due to laser heating, δx , is estimated by integrating the ion sound speed c_s over the time $\delta x = \int_{t_0}^t c_s(\tau) d\tau$ where the plasma neutrality is assumed. $t_0 = -75$ ps corresponds to the initial time and the sound speed is [30]

$$c_s = \sqrt{\frac{\gamma_e Z k_B T_e + \gamma_i k_B T_{il}}{m_i}}, \quad (17)$$

where $\gamma_e = 1$ and $\gamma_i = 3$ are the electron and ion heat capacity ratios, respectively [31]. The evolution of the ablator expansion during the solid-to-plasma transition is shown in Fig. 5.

Two main behaviors can be observed as for the electron density, electron temperature, and ion-lattice (see Fig. 1). If $t < 50$ ps, then the ion-lattice system remains cold and the ablator expansion is negligible (less than $0.1 \mu\text{m}$). If $t > 50$ ps, then the ion-lattice system is heated very quickly and reaches high temperatures in excess of several hundreds of eV. The ablator expansion, which may be of several μm , then has to be considered. Polystyrene ablators typically used in ICF experiments have a thickness of several tens of μm [32–34]. For $t \sim 70$ ps where the solid-to-plasma transition is mainly finished, the expansion is of the order of $1 \mu\text{m}$, i.e., less than 10% of the ablator thickness. We thus confirm that hydrodynamics can be neglected during the solid-to-plasma transition. However the solid-to-plasma transition may have an influence on the subsequent hydrodynamics as suggested in recent experiments to explain differences on the shock

velocities modulations between experimental and numerical results [11]. This discrepancy may be explained by the evolution of the matter pressure with the laser intensity which scales differently depending on the state of matter, thus forming different gradients responsible for shock formation and propagation.

V. SCALING LAW OF MATTER PRESSURE WITH RESPECT TO LASER INTENSITY

In above-mentioned experiments [11], shock velocities modulations induced in a polystyrene foil by a laser beam including speckles (spatial intensity modulations) were measured with a 2D VISAR to study the laser imprint. By using a state-of-the-art hydrocode assuming an initial plasma state, a good agreement of numerical simulations with experimental observations was obtained by increasing the intensity modulations by a factor of two. The later modification was supported by invoking the role of the initial solid state. By considering a fully ionized plasma, the relative pressure exerted by a beam profile, $\delta P/P$, is equal to the relative intensity variations $\delta I/I$. An ideal gas EOS is assumed with a constant density and a temperature resulting from linear laser absorption. Considering the initial solid state, absorption becomes nonlinear (ionization through two-photon absorption) and free electron density depends on laser intensity. Then $\delta P/P = \alpha \delta I/I$, or $P \propto I^\alpha$, where the coefficient α accounts for the plasma formation. Compared with an initial fully ionized plasma state, the solid-to-plasma transition is thus expected to modify the scaling law of the pressure as a function of the laser intensity. This section is devoted to the investigation of the modification of the previous scaling law exponent due to the solid-to-plasma transition.

First, the scaling law exponent is evaluated for a fully ionized plasma. The obtained value will be a reference to check the predictions of the present solid-to-plasma model. The total pressure p is given by considering electron and ion contributions, $p = p_e + p_i$, with p_e and p_i the electron and ion pressures, respectively. Assuming electrons and ions have the same temperature (long enough time) and ideal gas EOS, the total pressure reads

$$p = \left(1 + \frac{1}{Z}\right) n_e k_B T_e, \quad (18)$$

with $Z = n_e/n_i$ the averaged ionization degree of the plasma. Thus, the scaling law of the pressure as a function of the laser intensity is due to the evolutions of both electron density n_e and electron temperature T_e . For a fully ionized plasma where n_e is constant, only the electron temperature scaling needs to be evaluated. This is done by Eq. (1), which, after simplification, reads

$$\frac{\partial T_e}{\partial t} = \frac{16\pi e^2 v_c}{3ck_B m_e \omega_L^2} I_L(t), \quad (19)$$

with c the light velocity. $v_c \ll \omega_L$ is assumed for a hot enough plasma. Thus, the scaling law of the temperature is obtained owing to the scaling law of the electron collision frequency. The assumption of a hot plasma enables to write $v_c \propto T_e^{-3/2} \ln \Lambda$. Neglecting the electron temperature dependency of the Coulomb logarithm, the previous equation can be

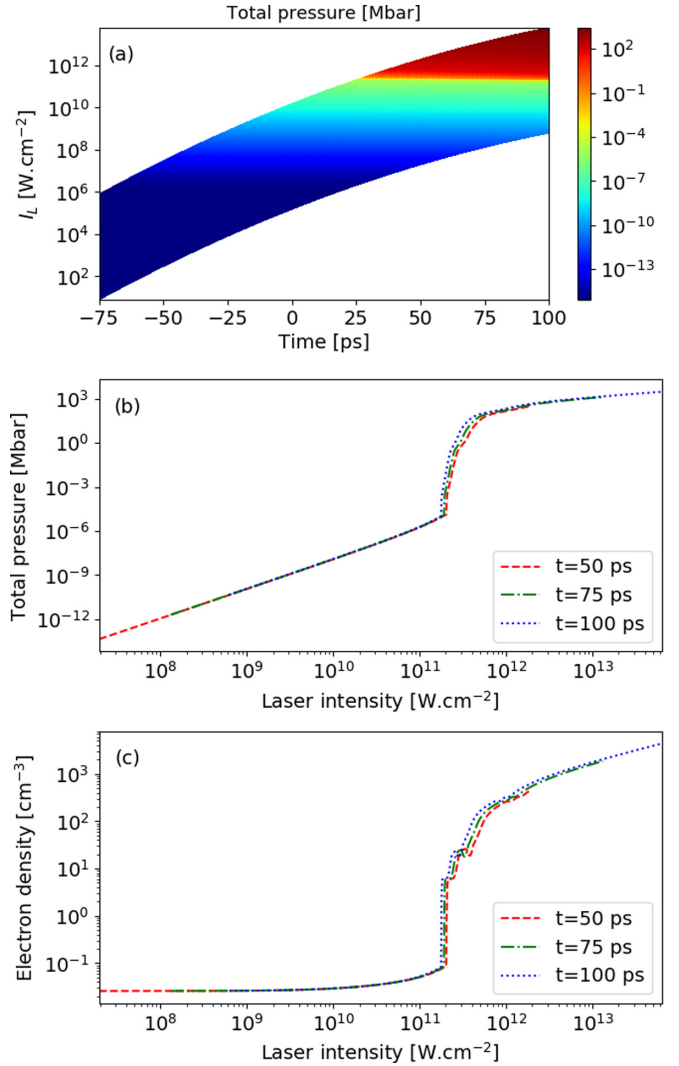


FIG. 6. (a) Total pressure as a function of time and of the laser intensity, (b) total pressure as a function of the laser intensity for three different instants, (c) electron density as a function of the laser intensity for three different instants.

solved leading to

$$T_e^{5/2} - T_0^{5/2} \propto I_0 F(t), \quad (20)$$

with T_0 the initial electron temperature and $F(t) = \int_{-\infty}^t f(t) dt$ where the laser intensity profile is $I_L(t) = I_0 f(t)$ where $f(t)$ is the temporal profile. With $T_0 \ll T_e$, the scaling law of the pressure as a function of the laser intensity for a fully ionized plasma reads

$$p \propto I_0^{2/5}. \quad (21)$$

To study the modification of this scaling law due to the solid-to-plasma transition, simulations were performed by using the model presented in Sec. II and a Gaussian shape for the temporal laser intensity profile with the same parameters as those used in Sec. III. Simulations were performed for different maximum laser intensities I_0 ranging from 10¹² W.cm⁻² to 10¹⁵ W.cm⁻². Figure 6 shows the evolution of the total pressure and the electron density as a function of time and of the laser intensity.

It can be observed on Fig. 6(b) that the pressure evolution exhibits four behaviors. The first three behaviors are related to the evolution of the electron density while the last one is related to the evolution of the electron temperature. When $I_L < 2.0 \times 10^{11} \text{ W.cm}^{-2}$, the ablator is solid polystyrene and the electron density scales as $n_e \propto I_L^2$ as shown by Fig. 6(c). This scaling law is also valid for the pressure, because the electron temperature remains relatively constant for the solid polystyrene state [see Fig. 1(b)]. In that case the scaling of the pressure is given by the scaling of the electron density. Thus, when $I_L < 2.0 \times 10^{11} \text{ W.cm}^{-2}$, the pressure scales as $p \propto I_L^2$. For laser intensities between $2.0 \times 10^{11} \text{ W.cm}^{-2}$ and $5.0 \times 10^{11} \text{ W.cm}^{-2}$, the pressure exhibits a fast increase which is due to the increase in the electron density induced by dissociations and ionizations of all molecular and atomic species present at this moment. A rough fit of the pressure leads to the following scaling law: $p_e \propto I_L^{11}$. For laser intensities between $6.0 \times 10^{11} \text{ W.cm}^{-2}$ and $2.0 \times 10^{12} \text{ W.cm}^{-2}$, the evolution of the pressure is due to the increase of the electron density going from $2.5 \times 10^{23} \text{ cm}^{-3}$ to $3.5 \times 10^{23} \text{ cm}^{-3}$. This evolution is due to the last two ionizations of carbon taking place for $I_L \approx 10^{12} \text{ W.cm}^{-2}$. A numerical fit leads to $p \propto I_L^{1.2}$. Finally, for $I_L > 3.0 \times 10^{12} \text{ W.cm}^{-2}$, the electron density remains constant and the evolution of the pressure is due to variations of electron temperature. In that case, a fitting of the pressure leads to $p \propto I_L^{0.5}$. This scaling law is similar to the one given by Eq. (21). The exponent difference (0.5 vs 0.4) is due to the dependence of the collision frequency on the electron temperature. Equation (21) has been obtained assuming a constant Coulomb logarithm, neglecting the electron-ion energy transfer, and assuming $v_c \ll \omega_L$ to evaluate the energy absorption, the last two assumptions leading to Eq. (19).

These results show that the solid-to-plasma transition strongly modifies the scaling law of the pressure as a function of the laser intensity due to the free electron generation. By fitting the curves over a relevant intensity range, the average scaling law exponent is of the order of 3. This work thus confirms *a posteriori* the approach discussed in Ref. [11] to account for experimental observations. Note that a similar experimental study has been carried out recently with different parameters [35] where the photoionization of the solid target is due to one-photon absorption. As in Ref. [11], state-of-the-art numerical simulations with an initial plasma state cannot account accurately of experimental observations. Since the primary ionization process of the solid plastic is due to a linear absorption process, the authors of Ref. [35] concluded that the introduction of the solid-to-plasma transition is not enough to explain discrepancies. Here we have shown that the scaling law exponent value is mainly due to variations of the free electron density, regardless the exact ionization process (of course the precise value of the exponent depends on the ionization processes). The solid-to-plasma transition may thus also mainly explain experimental and theoretical discrepancies observed in Ref. [35].

VI. CONCLUSION AND OUTLOOKS

An improved description of the solid-to-plasma transition has been proposed in this work enabling to investigate in particular the temporal evolution of the electron density,

electron temperature and ion-lattice temperature during the early interaction between the ablator and typical laser pickets used in ICF experiments. They exhibit two distinct behaviors associated to the chemical composition of the ablator. As long as the ion-lattice temperature is smaller than 58 meV, the ablator is in the solid polystyrene state. The electron density is driven by the laser-induced photoionization and the electron and ion-lattice temperatures are driven by collisions between electrons and phonons. For higher temperatures, polystyrene dissociates, transforming into various molecular and atomic species. The electron density is then driven by electron impact ionization while the heating of the electrons and of the ion-lattice system is driven by electron-ion collisions. This model leads to a non negligible solid-to-plasma transition timescale of about 100 ps, which is about the order of magnitude of laser pickets duration. The present model can estimate the density of carbon and hydrogen ions at the end of the solid-to-plasma transition, as well as electron and ion temperatures, which makes it suitable for its implementation in an ICF hydrocode.

The chemical evolution of the ablator going from polystyrene to a mixture of carbon and hydrogen atomic species has been investigated. It takes place over a period of time of about 10 ps, which is not negligible compared with the solid-to-plasma transition timescale. However, some intermediate chemical species are present only during a few ps and should be neglected for application purposes. By extrapolating the scenario of polystyrene fragmentation, a general scenario of fragmentation of plastics can be deduced. Indeed, in the ICF framework, and more generally within the laser-plasma interaction context, polystyrene is only one among a large number of plastics that can be used, in particular of the case of complex target coating or the use of foams [36–38]. We thus propose a simpler two-step scenario for the plasma formation: (i) The plastic (polymer) dissociates into monomers around the ceiling temperature; (ii) monomers dissociate into atomic species when the ion-lattice temperature is in between 3 and 8 eV which corresponds to the typical range of chemical binding energies.

Finally, by investigating the evolution of the matter pressure as a function of the laser intensity, we have shown that the strong modification of the scaling law exponent is due to the solid-to-plasma transition where the free electron density varies. The solid-to-plasma transition is thus expected to have a significant influence on the shock formation and propagation for the laser imprint issue, and on the shinethrough issue as already demonstrated with a simplified model [28]. To definitely confirm these expectations, the model presented in this work will be implemented in a state-of-the-art multidimensional radiative hydrodynamic code. By doing so, it will be possible in addition to determine whether the early-time evolution of the ablator has a significant influence on the target implosion and performance such as the neutral yield within direct-drive ICF conditions.

ACKNOWLEDGMENTS

The authors acknowledge Vladimir Tikhonchuk for his fruitful comments about this work. CEA is also acknowledged for supporting these studies. S.X.H. acknowledges the support by the U.S. Department of Energy National Nuclear Security

Administration under Award No. DE-NA0003856, the University of Rochester, and the New York State Energy Research and Development Authority.

APPENDIX A: TWO-TEMPERATURE MODEL WITH A NONCONSTANT NUMBER OF PARTICLES

Let us consider a thermodynamic system with a dependence on the number N of particles. Thus, the total differential of the energy U of the system reads [39]

$$dU = TdS - PdV + \mu dN, \quad (\text{A1})$$

where T , S , P , V , and μ are the temperature, entropy, pressure, volume and chemical potential, respectively. This equation leads to the definition of P and μ :

$$P = -\left(\frac{\partial U}{\partial V}\right)_{S,N}; \quad \mu = \left(\frac{\partial U}{\partial N}\right)_{S,V}. \quad (\text{A2})$$

By using the free energy F defined by $F = U - TS$, which its total differential is $dF = -SdT - PdV + \mu dN$, the entropy can be defined as $S = -(\partial F/\partial T)_{V,N}$. Because F is a function of T , V and N , the entropy is a function of these same variables and its total differential is

$$dS = \left(\frac{\partial S}{\partial T}\right)_{V,N} dT + \left(\frac{\partial S}{\partial V}\right)_{T,N} dV + \left(\frac{\partial S}{\partial N}\right)_{T,V} dN. \quad (\text{A3})$$

By substituting this expression for the differential of the entropy in Eq. (A1), this allows us to write the total derivative of the energy as

$$dU = C_v dT - \tilde{p} dV + \tilde{\mu} dN, \quad (\text{A4})$$

with $C_v = T(\partial S/\partial T)_{V,N}$ the heat capacity of a system with a variable number of particles as defined by Landau [39]. The partial derivatives over V and N have been gathered to defined an effective pressure \tilde{p} and an effective chemical potential $\tilde{\mu}$ as follows:

$$\tilde{p} = -\left(\frac{\partial U}{\partial V}\right)_{T,N} = P + T\left(\frac{\partial S}{\partial V}\right)_{T,N}, \quad (\text{A5})$$

$$\tilde{\mu} = \left(\frac{\partial U}{\partial N}\right)_{T,V} = \mu + T\left(\frac{\partial S}{\partial N}\right)_{T,V}. \quad (\text{A6})$$

Finally, the variations of internal energy is given by

$$\frac{\partial U}{\partial t} = C_v \frac{\partial T}{\partial t} - \tilde{p} \frac{\partial V}{\partial t} + \tilde{\mu} \frac{\partial N}{\partial t}. \quad (\text{A7})$$

APPENDIX B: THERMODYNAMIC QUANTITIES IN THE FREE ELECTRON GAS APPROXIMATION

The two electron thermodynamic quantities of interest in the two-temperature model are the electron heat capacity C_e and the effective chemical potential μ_{eff} . As the ablator does not significantly expand during its solid-to-plasma transition, the electron density can be very large. Thus, it is assumed electrons can be degenerated and the free electron gas approximation is used to recover both degenerate and nondegenerate regime. Thus, the electron energy reads

$$U_e = \frac{\sqrt{2}m_e^{3/2}}{\pi^2\hbar^3} \int_0^{+\infty} \frac{\varepsilon^{3/2}}{e^{(\varepsilon-\mu_e)/k_B T_e} + 1} d\varepsilon, \quad (\text{B1})$$

which can be written in terms of the complete Fermi-Dirac integral:

$$U_e = \frac{\sqrt{2}m_e^{3/2}}{\pi^2\hbar^3} (k_B T_e)^{5/2} F_{3/2}\left(\frac{\mu_e}{k_B T_e}\right). \quad (\text{B2})$$

According to Landau and Lifshitz [39], the heat capacity of a system with a variable number of particles is defined by $C_v = T(\partial S/\partial T)_{V,N}$. By using Eq. (A1) and the fact that T , V , and N are independent variables, this allows us to define C_v in terms of U_e :

$$C_v = \left(\frac{\partial U_e}{\partial T}\right)_{V,N}. \quad (\text{B3})$$

Thus, by using Eq. (B2), this leads to

$$C_v = \frac{\sqrt{2}m_e^{3/2}}{\pi^2\hbar^3} \left[\frac{5}{2} k_B^{5/2} T_e^{3/2} F_{3/2}\left(\frac{\mu_e}{k_B T_e}\right) + \frac{3}{2} (k_B T_e)^{5/2} F_{1/2}\left(\frac{\mu_e}{k_B T_e}\right) \frac{\partial}{\partial T_e} \left(\frac{\mu_e}{k_B T_e}\right) \right], \quad (\text{B4})$$

where the property of the Fermi-Dirac integral $dF_j(x)/dx = jF_{j-1}(x)$ has been used. Finally, as the electron density is defined by

$$n_e = \frac{\sqrt{2}m_e^{3/2}}{\pi^2\hbar^3} (k_B T_e)^{3/2} F_{1/2}\left(\frac{\mu_e}{k_B T_e}\right), \quad (\text{B5})$$

the heat capacity can be written as

$$C_v = \frac{3}{2} k_B n_e \left[\frac{5F_{3/2}(\mu_e/k_B T_e)}{3F_{1/2}(\mu_e/k_B T_e)} + T_e \frac{\partial}{\partial T_e} \left(\frac{\mu_e}{k_B T_e}\right) \right]. \quad (\text{B6})$$

Because n_e and T_e are independent variables, the derivative of n_e with respect to T_e is equal to 0. Thus, by calculating explicitly this derivative from Eq. (B5), we obtain

$$\frac{\partial}{\partial T_e} \left(\frac{\mu_e}{k_B T_e}\right) = -\frac{3}{T_e} \frac{F_{1/2}(\mu_e/k_B T_e)}{F_{-1/2}(\mu_e/k_B T_e)}, \quad (\text{B7})$$

and the heat capacity of electrons is finally given by

$$C_v = \frac{3}{2} k_B n_e \left[\frac{5F_{3/2}(\mu_e/k_B T_e)}{3F_{1/2}(\mu_e/k_B T_e)} - 3 \frac{F_{1/2}(\mu_e/k_B T_e)}{F_{-1/2}(\mu_e/k_B T_e)} \right]. \quad (\text{B8})$$

In the limit of the ideal gas, $\mu_e/k_B T_e \ll -1$. Thus, the Fermi-Dirac integral can be simplified to $F_j(x) \approx \Gamma(j+1)e^x$ with Γ the Gamma function, which leads to $C_v = 3k_B n_e/2$. In the limit $\mu_e/k_B T_e \gg 1$, the Fermi-Dirac integrals can be simplified owing to the Sommerfeld expansion leading to the heat capacity of the free electron gas $C_v \approx \pi^2 k_B^2 T_e n_e / 2\varepsilon_F$ [16].

Regarding the effective chemical potential μ_e , it comes directly:

$$\tilde{\mu}_e = \frac{3}{2} \frac{\sqrt{2}m_e^{3/2}}{\pi^2\hbar^3} (k_B T_e)^{3/2} F_{1/2}\left(\frac{\mu_e}{k_B T_e}\right) \frac{\partial \mu_e}{\partial n_e}, \quad (\text{B9})$$

inserting Eq. (B2) into Eq. (A6) and using the property $dF_j(x)/dx = jF_{j-1}(x)$. By calculating the derivative of n_e with respect to itself, one obtains

$$\frac{\partial n_e}{\partial n_e} = \frac{\sqrt{2}m_e^{3/2}}{\pi^2\hbar^3} \frac{k_B T_e}{2} F_{-1/2}\left(\frac{\mu_e}{k_B T_e}\right) \frac{\partial \mu_e}{\partial n_e}. \quad (\text{B10})$$

Obviously, this derivative is also equal to unity and it is possible to have an expression of $\partial\mu_e/\partial n_e$. Inserting this expression into Eq. (B9), the effective chemical potential is finally

given by

$$\tilde{\mu}_e = 3k_B T_e \frac{F_{1/2}(\mu_e/k_B T_e)}{F_{-1/2}(\mu_e/k_B T_e)}. \quad (\text{B11})$$

APPENDIX C: ELECTRON-PHONON ENERGY TRANSFER

Following the theory developed by Allen [40], the energy transfer resulting from a collision between an electron and an acoustic or optical phonon is defined by

$$\frac{\partial E_e}{\partial t} = \frac{4\pi}{\hbar} \sum_{\mathbf{k}, \mathbf{k}'} \hbar\omega_{\mathbf{q}} |M_{\mathbf{k}, \mathbf{k}'}|^2 S(\mathbf{k}, \mathbf{k}') \delta(\varepsilon_{\mathbf{k}} - \varepsilon_{\mathbf{k}'} + \hbar\omega_{\mathbf{q}}). \quad (\text{C1})$$

The term $S(\mathbf{k}, \mathbf{k}')$ corresponds to the so-called thermal factor, $\varepsilon_{\mathbf{k}}$ and $\varepsilon_{\mathbf{k}'}$ are electron energies in states \mathbf{k} and \mathbf{k}' , respectively, and $\hbar\omega_{\mathbf{q}}$ is the phonon energy absorbed or emitted by the electron moving from the state \mathbf{k} to the state \mathbf{k}' , and satisfying the momentum conservation $\mathbf{k}' = \mathbf{k} + \mathbf{q}$. As the matrix element $|M_{\mathbf{k}, \mathbf{k}'}|^2$ given by [41]

$$|M_{\mathbf{k}, \mathbf{k}'}|^2 = -\frac{\hbar}{2\rho V \omega_{\mathbf{q}}} (n_{\mathbf{q}} + 1) q^2 \mathcal{U}^2(\omega_{\mathbf{q}}, \mathbf{q}) \delta(\mathbf{k} - \mathbf{k}' + \mathbf{q}), \quad (\text{C2})$$

with $n_{\mathbf{q}} = [\exp(\hbar\omega_{\mathbf{q}}/k_B T_{il}) - 1]^{-1}$ the Bose-Einstein distribution and $\mathcal{U}(\omega_{\mathbf{q}}, \mathbf{q})$ the deformation potential. By writing the energy conservation as

$$\delta(\varepsilon_{\mathbf{k}} - \varepsilon_{\mathbf{k}'} + \hbar\omega_{\mathbf{q}}) = \frac{m_e}{\hbar^2 k q} \delta\left(\cos\theta - \frac{m_e \omega_{\mathbf{q}}}{\hbar k q} - \frac{q}{2k}\right), \quad (\text{C3})$$

with θ the angle between \mathbf{k} and \mathbf{q} , where it was used the momentum conservation $\mathbf{k}' = \mathbf{k} + \mathbf{q}$ and assumed a free electron gas, i.e., $\varepsilon_{\mathbf{k}} = \hbar^2 \mathbf{k}^2 / m_e$. This allows us to write Eq. (C1) as follows:

$$\frac{\partial \mathcal{E}_e}{\partial t} = -\frac{2\pi}{(8\pi^3)^2} \int \left\{ \int \left[\frac{m_e q}{\rho \hbar k} (n_{\mathbf{q}} + 1) \mathcal{U}^2(\omega_{\mathbf{q}}, \mathbf{q}) S(\mathbf{k}, \mathbf{k}') \delta\left(\cos\theta - \frac{m_e \omega_{\mathbf{q}}}{\hbar k q} - \frac{q}{2k}\right) \right] d\mathbf{k}' \right\} d\mathbf{k}. \quad (\text{C4})$$

Note that $\sum_{\mathbf{k}} = (V/8\pi^3) \int d\mathbf{k}$ has been used assuming close enough electron states and the electron energy E_e has been replaced by the electron energy per unit volume $\mathcal{E}_e = E_e/V$. The thermal factor $S(\mathbf{k}, \mathbf{k}')$ is defined by $S(\mathbf{k}, \mathbf{k}') = [f(\varepsilon_{\mathbf{k}}) - f(\varepsilon_{\mathbf{k}'})] n_{\mathbf{q}} - f(\varepsilon_{\mathbf{k}'}) [1 - f(\varepsilon_{\mathbf{k}})]$ with $f(\varepsilon_{\mathbf{k}}) = \{\exp[(\varepsilon_{\mathbf{k}} - \mu_e)/k_B T_e] + 1\}^{-1}$ the Fermi-Dirac distribution but can be written as

$$S(\mathbf{k}, \mathbf{k}') = [f(\varepsilon_{\mathbf{k}}) - f(\varepsilon_{\mathbf{k}} + \hbar\omega_{\mathbf{q}})] [n_{\mathbf{q}}(T_{il}) - n_{\mathbf{q}}(T_e)], \quad (\text{C5})$$

so that it clearly appears $S(\mathbf{k}, \mathbf{k}') = 0$ and $\partial_t E_e = 0$ when $T_e = T_{il}$.

Owing to momentum conservation, integration over \mathbf{k}' can be replaced by integration over \mathbf{q} , which gives

$$\int d\mathbf{k}' = \int d\mathbf{q} = 2\pi \int_0^{+\infty} \int_{-1}^1 q^2 dq d\cos\theta, \quad (\text{C6})$$

and Eq. (C4) can be simplified after integration over $\cos\theta$ in terms of the Heaviside step function Θ as follows:

$$\begin{aligned} \frac{\partial \mathcal{E}_e}{\partial t} &= \frac{1}{16\pi^4} \int \left\{ \int_0^{+\infty} \left[\frac{m_e q^3}{\rho \hbar k} (n_{\mathbf{q}} + 1) \mathcal{U}^2(\omega_{\mathbf{q}}, \mathbf{q}) [f(\varepsilon_{\mathbf{k}}) - f(\varepsilon_{\mathbf{k}} + \hbar\omega_{\mathbf{q}})] [n_{\mathbf{q}}(T_e) - n_{\mathbf{q}}(T_{il})] \right. \right. \\ &\quad \left. \left. \times \Theta\left(1 - \frac{m_e \omega_{\mathbf{q}}}{\hbar k q} - \frac{q}{2k}\right) \Theta\left(1 + \frac{m_e \omega_{\mathbf{q}}}{\hbar k q} + \frac{q}{2k}\right) \right] dq \right\} d\mathbf{k}. \end{aligned} \quad (\text{C7})$$

1. Acoustic phonon

For acoustic phonons, the relation dispersion leads to $\omega_{\mathbf{q}} = c_s q$ with c_s the speed of sound and the deformation potential is a constant [41] $\mathcal{U}(\omega_{\mathbf{q}}, \mathbf{q}) = \mathcal{U}$. Thus, Eq. (C7) becomes

$$\frac{\partial \mathcal{E}_e}{\partial t} = \frac{1}{16\pi^4} \frac{m_e \mathcal{U}^2}{\rho \hbar} \int \left\{ \frac{1}{k} \int_0^{2k+2m_e c_s/\hbar} q^3 [n(\hbar c_s q, T_{il}) + 1] [f(\varepsilon_{\mathbf{k}}) - f(\varepsilon_{\mathbf{k}} + \hbar c_s q)] [n(\hbar c_s q, T_e) - n(\hbar c_s q, T_{il})] dq \right\} d\mathbf{k}. \quad (\text{C8})$$

As it appears that the integral over \mathbf{k} depends only on its modulus, one has $\int d\mathbf{k} = 4\pi \int_0^{+\infty} k^2 dk$ and the previous equation can be simplified into

$$\frac{\partial \mathcal{E}_e}{\partial t} = \frac{1}{4\pi^3} \frac{m_e \mathcal{U}^2}{\rho \hbar} \int_0^{k_{\text{BZ}}} \left\{ k \int_0^{2k+2m_e c_s/\hbar} q^3 [n(\hbar c_s q, T_{il}) + 1] [f(\varepsilon_{\mathbf{k}}) - f(\varepsilon_{\mathbf{k}} + \hbar c_s q)] [n(\hbar c_s q, T_e) - n(\hbar c_s q, T_{il})] dq \right\} d\mathbf{k}, \quad (\text{C9})$$

where the integration is restricted to the first Brillouin zone as during the solid-to-plasma transition, the electron energy does not exceed $E(k_{BZ})$. In the limit of small momentum transfer, one has $\hbar c_s q \ll k_B T_{il}$, and the Bose-Einstein distribution simplifies as $n(T_{il}) + 1 \approx k_B T_{il} / \hbar c_s q$ and $n(T_e) - n(T_{il}) \approx k_B (T_e - T_{il}) / \hbar c_s q$. Thus, Eq. (C9) becomes

$$\frac{\partial \mathcal{E}_e}{\partial t} = \frac{1}{4\pi^3} \frac{m_e k_B^2 \mathcal{U}^2 T_{il}}{\rho c_s^2 \hbar^3} (T_e - T_{il}) \int_0^{k_{BZ}} \left\{ k \int_0^{2k+2m_e c_s / \hbar} q [f(\varepsilon_k) - f(\varepsilon_k + \hbar c_s q)] dq \right\} dk. \quad (C10)$$

Finally, the energy transfer can be written in such a way that the electron-acoustic phonon energy transfer rate v_{et} appears:

$$\frac{\partial \mathcal{E}_e}{\partial t} = v_{et} n_e k_B (T_e - T_{il}), \quad (C11)$$

where v_{et} is defined by

$$v_{et} = \frac{1}{n_e} \frac{m_e k_B \mathcal{U}^2 T_{il}}{4\pi^3 \rho c_s^2 \hbar^3} \int_0^{k_{BZ}} k \times I \left(2k + 2 \frac{m_e c_s}{\hbar} \right) dk. \quad (C12)$$

The function I corresponds to the integral over q in Eq. (C10) and can be calculated analytically, leading to

$$I(\kappa) = \frac{\kappa^2}{2} - \frac{k_B T_{il}}{\hbar c_s} \kappa \log \left[1 + \exp \left(\frac{\varepsilon_\kappa + \hbar c_s \kappa - \mu_e}{k_B T_{il}} \right) \right] + \frac{k_B^2 T_{il}^2}{\hbar^2 c_s^2} \left[F_1 \left(\frac{\varepsilon_\kappa + \hbar c_s \kappa - \mu_e}{k_B T_{il}} \right) - F_1 \left(\frac{\varepsilon_\kappa - \mu_e}{k_B T_{il}} \right) \right], \quad (C13)$$

with $\varepsilon_\kappa = \hbar^2 \kappa^2 / 2m_e$. F_1 is the Fermi-Dirac integral of order 1.

2. Optical phonon

For optical phonons, the dispersion relation leads to $\omega_{\mathbf{q}} = \omega_{LO}$ and the deformation potential is given by the Fröhlich formalism [41–43]:

$$\mathcal{U}^2(\omega_{\mathbf{q}}, \mathbf{q}) = 4\pi e^2 \rho \omega_{LO}^2 \left(\frac{1}{\varepsilon_r^\infty} - \frac{1}{\varepsilon_r^0} \right) \frac{1}{q^4}, \quad (C14)$$

where ε_r^0 and ε_r^∞ are the dielectric constants at low and high frequencies, respectively. Plugging them into Eq. (C7) gives after integration over q :

$$\frac{\partial \mathcal{E}_e}{\partial t} = \frac{1}{4\pi^3} \frac{m_e e^2 \omega_{LO}^2}{\hbar} \left(\frac{1}{\varepsilon_r^\infty} - \frac{1}{\varepsilon_r^0} \right) [n(T_{il}) + 1] [n(T_e) - n(T_{il})] \int \left\{ \frac{1}{k} [f(\varepsilon_k) - f(\varepsilon_k + \hbar \omega_{LO})] \ln \left(\frac{k + \sqrt{k^2 - 2m_e \omega_{LO} / \hbar}}{k - \sqrt{k^2 - 2m_e \omega_{LO} / \hbar}} \right) \right\} d\mathbf{k}. \quad (C15)$$

As for acoustic phonons, the integration over \mathbf{k} depends only on its modulus leading, for the electron-optical phonon energy transfer, to

$$\frac{\partial \mathcal{E}_e}{\partial t} = \frac{m_e^2 e^2 \omega_{LO}^2}{\pi^2 \hbar^3} \left(\frac{1}{\varepsilon_r^\infty} - \frac{1}{\varepsilon_r^0} \right) [n(T_{il}) + 1] [n(T_e) - n(T_{il})] \int_{\hbar \omega_{LO}}^{E(k_{BZ})} [f(\varepsilon_k) - f(\varepsilon_k + \hbar \omega_{LO})] \ln \left(\frac{1 + \sqrt{1 - \hbar \omega_{LO} / \varepsilon_k}}{1 - \sqrt{1 - \hbar \omega_{LO} / \varepsilon_k}} \right) d\varepsilon_k \quad (C16)$$

after having transformed integration over k to integration over ε_k . Finally, as for acoustic phonons, it is possible to exhibit an electron-optical phonon energy transfer rate defined by

$$v_{et} = \frac{1}{n_e} \frac{m_e^2 e^2 \omega_{LO}^2}{\pi^2 \hbar^4} \left(\frac{1}{\varepsilon_r^\infty} - \frac{1}{\varepsilon_r^0} \right) (n(T_{il}) + 1) \int_{\hbar \omega_{LO}}^{E(k_{BZ})} [f(\varepsilon_k) - f(\varepsilon_k + \hbar \omega_{LO})] \ln \left(\frac{1 + \sqrt{1 - \hbar \omega_{LO} / \varepsilon_k}}{1 - \sqrt{1 - \hbar \omega_{LO} / \varepsilon_k}} \right) d\varepsilon_k, \quad (C17)$$

giving the following electron-optical phonon energy transfer:

$$\frac{\partial \mathcal{E}_e}{\partial t} = v_{et} \hbar \omega_{LO} n_e [n(T_e) - n(T_{il})]. \quad (C18)$$

[1] J. Nuckolls, L. Wood, A. Thiessen, and G. Zimmerman, *Nature (London)* **239**, 139 (1972).

[2] D. D. Meyerhofer, R. L. McCrory, R. Betti, T. R. Boehly, D. T. Casey, T. J. B. Collins, R. S. Craxton, J. A. Delettrez, D. H. Edgell, R. Epstein, K. A. Fletcher, J. A. Frenje, Y. Y. Glebov,

V. N. Goncharov, D. R. Harding, S. X. Hu, I. V. Igumenshchev, J. P. Knauer, C. K. Li, J. A. Marozas *et al.*, *Nucl. Fusion* **51**, 053010 (2011).

[3] V. N. Goncharov, T. C. Sangster, R. Betti, T. R. Boehly, M. J. Bonino, T. J. B. Collins, R. S. Craxton, J. A. Delettrez, D. H.

- Edgell, R. Epstein, R. K. Follett, C. J. Forrest, D. H. Froula, V. Yu. Glebov, D. R. Harding, R. J. Henchen, S. X. Hu, I. V. Igumenshchev, R. Janezic, J. H. Kelly *et al.*, *Phys. Plasmas* **21**, 056315 (2014).
- [4] R. Craxton, K. Anderson, T. Boehly, V. Goncharov, D. Harding, J. Knauer, M. McCrory, P. McKenty, D. Meyerhofer, J. Myatt, A. Schmitt, J. Sethian, R. Short, S. Skupsky, W. Theobald, W. Kruer, K. Tanaka, R. Betti, T. Collins, J. Delettrez *et al.*, *Phys. Plasmas* **22**, 110501 (2015).
- [5] G. Duchateau, S. X. Hu, A. Pineau, A. Kar, B. Chimier, A. Casner, V. Tikhonchuk, V. N. Goncharov, P. B. Radha, and E. M. Campbell, *Phys. Rev. E* **100**, 033201 (2019).
- [6] R. Ishizaki and K. Nishihara, *Phys. Rev. Lett.* **78**, 1920 (1997).
- [7] S. Bodner, *Phys. Rev. Lett.* **33**, 761 (1974).
- [8] P. B. Radha, V. N. Goncharov, T. J. B. Collins, J. A. Delettrez, Y. Elbaz, V. Y. Glebov, R. L. Keck, D. E. Keller, J. P. Knauer, J. A. Marozas, F. J. Marshall, P. W. McKenty, D. D. Meyerhofer, S. P. Regan, T. C. Sangster, D. Shvarts, S. Skupsky, Y. Srebro, R. P. J. Town, and C. Stoeckl, *Phys. Plasmas* **12**, 032702 (2005).
- [9] S. X. Hu, P. B. Radha, J. A. Marozas, R. Betti, T. J. B. Collins, R. S. Craxton, J. A. Delettrez, D. H. Edgell, R. Epstein, V. N. Goncharov, I. V. Igumenshchev, F. J. Marshall, R. L. McCrory, D. D. Meyerhofer, S. P. Regan, T. C. Sangster, S. Skupsky, V. A. Smalyuk, Y. Elbaz, and D. Shvarts, *Phys. Plasmas* **16**, 112706 (2009).
- [10] S. X. Hu, L. A. Collins, V. N. Goncharov, J. D. Kress, R. L. McCrory, and S. Skupsky, *Phys. Plasmas* **23**, 042704 (2016).
- [11] J. L. Peebles, S. X. Hu, W. Theobald, V. N. Goncharov, N. Whiting, P. M. Celliers, S. J. Ali, G. Duchateau, E. M. Campbell, T. R. Boehly, and S. P. Regan, *Phys. Rev. E* **99**, 063208 (2019).
- [12] A. Pineau, B. Chimier, S. X. Hu, and G. Duchateau, *Phys. Plasmas* **27**, 092703 (2020).
- [13] Y. Lee and R. More, *Phys. Fluids* **27**, 1273 (1984).
- [14] C. A. Ordonez and M. I. Molina, *Phys. Rev. Lett.* **72**, 2407 (1994).
- [15] U. Gaur and B. Wunderlich, *J. Phys. Chem. Ref. Data* **11**, 313 (1982).
- [16] N. Ashcroft and N. Mermin, *Physique des Solides* (EDP Sciences, Les Ulis, France, 2002).
- [17] S. Atzeni and J. Meyer-ter Vehn, *The Physics of Inertial Fusion* (Clarendon Press, Oxford, 2004).
- [18] S. X. Hu, L. A. Collins, V. N. Goncharov, J. D. Kress, R. L. McCrory, and S. Skupsky, *Phys. Rev. E* **92**, 043104 (2015).
- [19] V. Sangawar and M. Golchha, *Int. J. Sci. Eng. Res.* **4**, 2700 (2013).
- [20] B. Arad and S. Eliezer, *Phys. Rev. A* **18**, 2261 (1978).
- [21] B. Rethfeld, *Phys. Rev. Lett.* **92**, 187401 (2004).
- [22] L. V. Keldysh, *Sov. Phys. JETP* **20**, 1307 (1965).
- [23] M. Chergui, *Femtochemistry, Ultrafast Chemical and Physical Processes on Molecular Systems* (World Scientific, Singapore, 1995).
- [24] M. Gryziński, *Phys. Rev.* **138**, A336 (1965).
- [25] Y. B. Zel'dovich and Y. P. Raizer, *Physics of Shock Waves and High-Temperature Hydrodynamic Phenomena*, edited by W. D. Hayes and R. F. Probstein (Academic Press, San Diego, CA, 1966).
- [26] E. M. Lifshitz and L. P. Pitaevskii, *Course of Theoretical Physics. Volume 10: Physical Kinetics* (Butterworth-Heinemann, Oxford, UK, 1981).
- [27] V. N. Goncharov, T. C. Sangster, T. R. Boehly, S. X. Hu, I. V. Igumenshchev, F. J. Marshall, R. L. McCrory, D. D. Meyerhofer, P. B. Radha, W. Seka, S. Skupsky, C. Stoeckl, D. T. Casey, J. A. Frenje, and R. D. Petrasso, *Phys. Rev. Lett.* **104**, 165001 (2010).
- [28] A. Kar, S. X. Hu, G. Duchateau, J. Carroll-Nellenback, and P. B. Radha, *Phys. Rev. E* **101**, 063202 (2020).
- [29] D. H. Edgell, W. Seka, R. E. Bahr, T. R. Boehly, and M. J. Bonino, *Phys. Plasmas* **15**, 092704 (2008).
- [30] L. Spitzer, *Physics of Fully Ionized Gases* (Interscience Publishers, Geneva, 1956).
- [31] W. Kruer, *The Physics Of Laser Plasma Interactions* (CRC Press, Boca Raton, FL, 2003).
- [32] J. D. Lindl, *Phys. Plasmas* **2**, 3933 (1995).
- [33] V. N. Goncharov, J. P. Knauer, P. W. McKenty, P. B. Radha, T. C. Sangster, S. Skupsky, R. Betti, R. L. McCrory, and D. D. Meyerhofer, *Phys. Plasmas* **10**, 1906 (2003).
- [34] S. X. Hu, V. N. Goncharov, T. R. Boehly, R. L. McCrory, S. Skupsky, L. A. Collins, J. D. Kress, and B. Militzer, *Phys. Plasmas* **22**, 056304 (2015).
- [35] J. Oh, A. J. Schmitt, M. Karasik, and S. P. Obenschain, *Phys. Plasmas* **28**, 032704 (2021).
- [36] H. Nishimura, H. Shiraga, H. Azechi, N. Miyanaga, M. Nakai, N. Izumi, M. Nishikino, M. Heya, K. Fujita, Y. Ochi, K. Shigemori, N. Ohnishi, M. Murakami, K. Nishihara, R. Ishizaki, H. Takabe, K. Nagai, T. Norimatsu, M. Nakatsuka, T. Yamanaka *et al.*, *Nucl. Fusion* **40**, 547 (2000).
- [37] S. Depierreux, C. Labaune, D. T. Michel, C. Stenz, P. Nicolai, M. Grech, G. Riazuelo, S. Weber, C. Riconda, V. T. Tikhonchuk, P. Loiseau, N. G. Borisenko, W. Nazarov, S. Hüller, D. Pesme, M. Casanova, J. Limpouch, C. Meyer, P. Di-Nicola, R. Wrobel *et al.*, *Phys. Rev. Lett.* **102**, 195005 (2009).
- [38] S. Y. Guskov, J. Limpouch, P. Nicolai, and V. T. Tikhonchuk, *Phys. Plasmas* **18**, 103114 (2011).
- [39] L. D. Landau and E. M. Lifshitz, *Course of Theoretical Physics. Volume 5: Statistical Physics 3rd Edition Part 1* (Butterworth-Heinemann, Oxford, UK, 1980).
- [40] P. Allen, *Phys. Rev. Lett.* **59**, 1460 (1987).
- [41] J. Ziman, *Electrons and Phonons*, edited by N. Mott, E. Bullard, and D. Wilkinson (Clarendon Press, Oxford, UK, 1960).
- [42] H. Fröhlich, H. Pelzer, and S. Zienau, *Philos. Mag. Ser. 7* **41**, 221 (1950).
- [43] F. Guistino, *Rev. Mod. Phys.* **89**, 015003 (2017).